

# Optical Probe for Monitoring Blade Tip Clearance

Andrei B. Vakhtin<sup>1</sup>, Shin-Juh Chen<sup>2</sup>, and Steve M. Massick<sup>3</sup>  
*Southwest Sciences, Inc., 1570 Pacheco Street, Suite E-11, Santa Fe, NM 87505*

The reduction of blade tip clearance in high pressure turbine (HPT) and high pressure compressor (HPC) engines, defined as the void between a blade tip and the surrounding casing, has been a subject of intense research since the inception of the gas turbine engine. A prototype sensor based on an interferometric ranging technique, was built and tested for monitoring tip clearances. The method provided measurement accuracy of better than 10 micrometers. It is robust, inherently self-calibrating, and insensitive to environmental variations. The performance of the sensor was evaluated in both room temperature and inside a tube furnace to simulate the turbine environment. The spatial resolution, clearance measurement accuracy, clearance measurement range, and sensitivity of the prototype sensor were determined. The sensor system will provide a new tool for engine manufacturers to study and optimize blade tip clearance with high accuracy without the need for repetitive and cumbersome calibration procedures.

## Nomenclature

$N$	=	number of pixels in the detector array
$LO$	=	local oscillator
$R$	=	reflected light intensity
$k$	=	optical wavenumber
$\lambda$	=	laser wavelength
$\lambda_c$	=	center laser wavelength

## I. Introduction

MINIMIZATION of blade tip clearance in the high pressure turbine (HPT) and high pressure compressor (HPC), defined as the void between a blade tip and the surrounding casing, has been a subject of intense research since the inception of the gas turbine engine. The benefits of reduced tip clearance include the increase of turbine efficiency which reduces the amount of fuel burned and lowers the rotor inlet temperature, the reduction of emissions as the result of burning less fuel, the extension of service life due to lower operating temperature, the increase in payload, and the extension of mission range capabilities [1]. Unfortunately, engine loads, flight loads, and wear mechanisms on both stationary and rotating structures generate asymmetric and axisymmetric changes in tip clearance [2]. Engine loads encompass centrifugal, thermal, internal, engine pressure, and thrust loads. Flight loads include inertial (due to gravity), aerodynamic (due to external pressure), and gyroscopic loads. The sources of wear mechanisms are rubbing (blade incursion), erosion, and thermal fatigue. In addition, tip clearances vary due to engine operating points (i.e., takeoff, ground idle, cruise, acceleration, etc.) and engine life cycle.

A robust real-time clearance measurement technology for high temperature turbine applications capable of operating in the harsh environment of the gas generator and power turbine over the full range of operation, including extreme temperatures (up to 2000°F) and severe electrical disturbances is needed. Integrated into multiple engine manufacturers' military engine development efforts, this technology will reduce engine development cycle time and cost by enabling turbine clearances to be understood and optimized to achieve improved engine fuel efficiency and durability. Integrated into engine manufacturer's future turbine engines it will attain improved engine fuel efficiency on future advanced military or commercial engine development programs or on upgrades to current fielded systems.

---

<sup>1</sup> Currently with Vista Photonics.

<sup>2</sup> Senior Research Scientist, Corresponding Author, AIAA Member.

<sup>3</sup> Senior Research Scientist.

An innovative approach based on optical low coherence reflectometry is used. The method will provide a 10- $\mu\text{m}$  (or better) tip clearance measurement accuracy; it will be robust, inherently self-calibrating and insensitive to environmental variations. Ultimately, sensors could be mounted around the circumference of the inner housing (or blade outer air seal, BOAS) of the hot turbine section. The high temperature sensors will be very simple and interchangeable with existing (e.g., capacitance) sensors. The optical windows of the sensors will be flush-mounted with the inside surface of BOAS, so that the gas flow is not disturbed. The target instrument will be robust, and will provide near real-time mapping of blade-tip clearances measured at several points along the BOAS circumference.

## II. Tip Clearance Measurement Techniques

### A. Current Methods

The methods currently used for turbine blade tip clearance measurement are capacitive measurement methods, radar-type measurements using microwave electromagnetic waves, and laser Doppler velocimetry. The capacitance sensors are the most common. They provide measurement accuracy of about 50  $\mu\text{m}$ ; however this accuracy appears to be not sufficient given the typical clearance range of 250–750  $\mu\text{m}$ . Microwave interferometric techniques [3] allow real-time tip-clearance measurements with an accuracy of about 20  $\mu\text{m}$ . The microwave technique is very sensitive to the geometry of the sensor environment which results in the need to calibrate the instrument for each particular measurement. Also, since the microwave sensor probe itself is a hollow rf wave guide, the gas flow in the turbine may be disturbed. With laser Doppler velocimetry, tip-clearance measurements with a 20  $\mu\text{m}$  accuracy have been reported [4]. However, the Doppler sensor head contains relatively complex optics that require water cooling.

The technique we present here is based on an interferometric ranging technique — optical Fourier domain reflectometry (OFDR). This method is capable of real-time (or near-real-time) tip-clearance measurements with an accuracy of 10  $\mu\text{m}$  or better. It involves a simple high-temperature measurement sensor head comprised of a high temperature fiber and a robust common path interferometer. The principle of OFDR is discussed below.

### B. Optical Fourier Domain Reflectometry (OFDR)

Optical Fourier domain reflectometry is a powerful technique for ranging, surface profiling, and characterization of optical fibers and components. It is closely related to Fourier domain optical coherence tomography (FD-OCT), which is used for imaging internal structures of translucent objects, mostly in biomedical applications. With these imaging technologies, spatial resolutions of up to a few micrometers and sensitivities up to 160 dB have been achieved [5]. For micrometer-scale resolution, the measurement range is generally several millimeters.

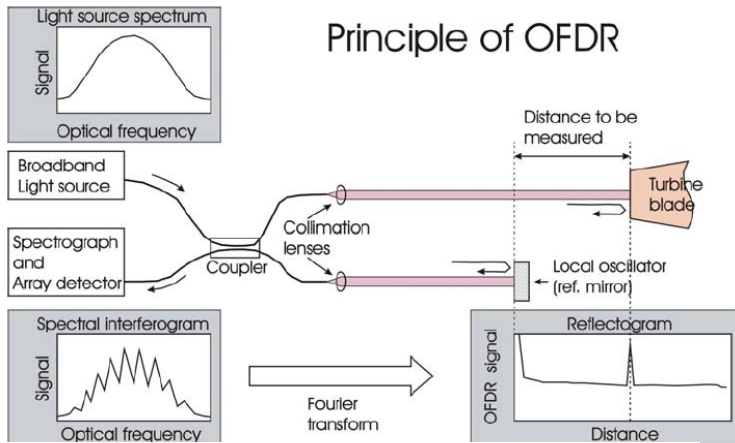


**Figure 1. Principle of OFDR**

coming from the sample at a distance  $z$  from the LO the spectral interferogram  $I$  can be expressed as follows:

$$I(z, k) = I_0 (R_{LO} R(z))^{1/2} \cos(2nkz - \phi) \quad (1)$$

where  $k$  is the optical wavenumber,  $k = 2\pi/\lambda$ ;  $\lambda$  is the wavelength;  $n$  is the effective index of refraction of the medium ( $n \approx 1$  for gas media);  $R_{LO}$  and  $R(z)$  are the reflection coefficients of the LO and the measured reflection, respectively;  $I_0$  is the light source intensity, and  $\phi$  is the arbitrary phase. Equation (1) shows that, for a reflection at a given distance  $z$ , the spectral interferogram is represented by a sinusoidal function of  $k$ . The frequency of the sinusoid is determined by the optical path difference between the reflection and the LO. The inverse Fourier transform applied to the interferogram converts the frequency of the fringes into the distance between the LO and the reflecting surface of the sample.

Our estimates show that the index of refraction of the gas medium at 2000°F does not deviate from unity by more than 0.5% ( $n - 1 < 0.005$ ) within the pressure range of 0–20 atm; therefore, we consider its effect negligible and omit  $n$  from subsequent equations.

The axial spatial resolution,  $\Delta z$ , is determined by the spectral bandwidth,  $\Delta\lambda$ , and center wavelength,  $\lambda_c$ , of the light source. A broader spectral bandwidth provides a shorter coherence length. Since interference occurs only within the coherence length, the axial resolution improves with greater spectral bandwidth:

$$\Delta z = (2 \ln 2 / \pi) (\lambda_c^2 / \Delta \lambda) \quad (2)$$

The axial spatial range,  $z_{\max}$ , is determined by the spectral resolution of the spectrometer/detector system:

$$z_{\max} = (1/\lambda_{\min} - 1/\lambda_{\max})^{-1} (N - 1)/4, \quad (3)$$

where  $\lambda_{\min}$  and  $\lambda_{\max}$  determine the spectral window of the spectrograph;  $N$  is the number of pixels in the detector array. Simply understood, reflection at greater distance produces higher frequency fringes. Thus, the maximum range is determined by the fringe resolution capability of the detection system. Equations (1-3) show that the OFRD method is self-calibrating: the absolute distance is determined from the spectral interferogram directly, without any assumptions or calibration.

### C. Common Path Interferometry

The system used here is a common path interferometer. Figure 2 schematically compares a traditional Michelson interferometer to a common path interferometer. A common path interferometer does not require a separate reference mirror for the LO. This permits a simpler design with fewer optical components. The sample and reference beams share the same optical path; the outer surface of a thick optical window (or lens) at the probe fiber tip serves as the LO. In a recent study, the common path interferometer was shown to be more stable and robust, much easier to align, providing automatic dispersion compensation, and significantly less sensitive to mechanical vibrations [10].

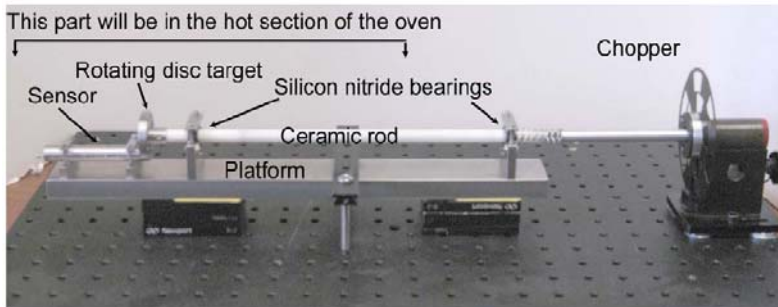


Figure 3. Experimental setup.

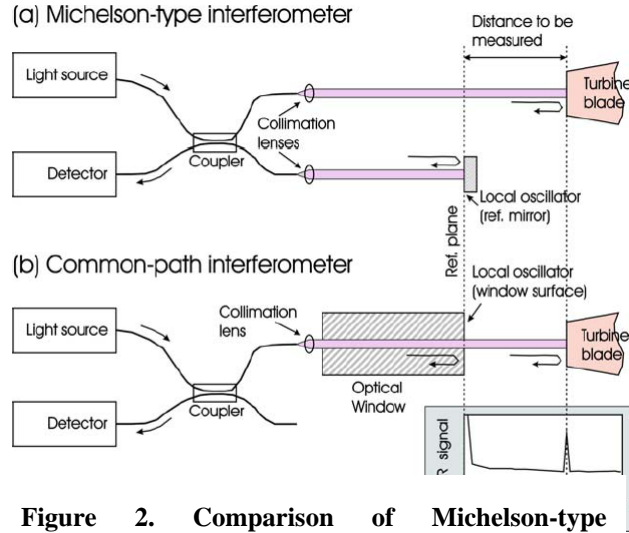
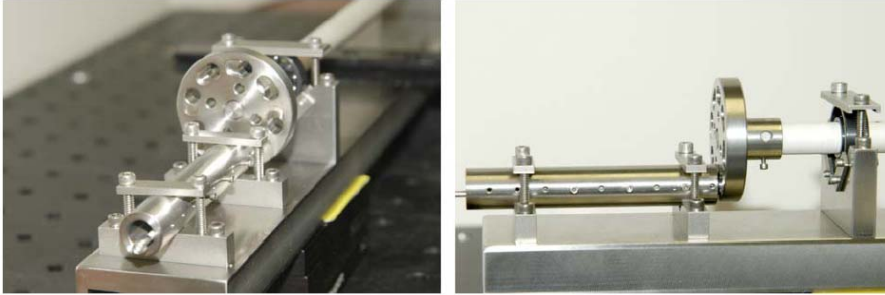


Figure 2. Comparison of Michelson-type interferometer and common-path interferometer.

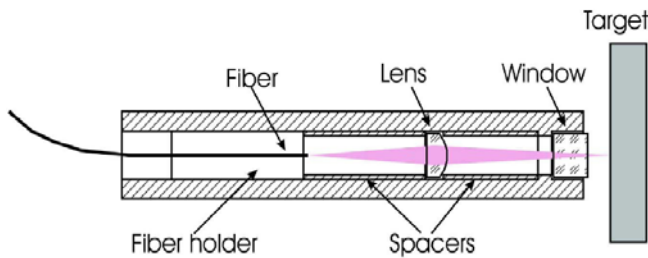
### III. Experimental Setup

Figure 3 shows the OFDR experimental setup comprising of a sensor head, rotating disk target, and a chopper wheel assembly. These components are made of high-temperature materials, such as stainless steel and ceramics. A ceramic rod connects the disc target to the chopper wheel. The chopper wheel is used to rotate the disc target at a specified rotational speed. Two all-silicon-nitride bearings hold the ceramic rod in place and allow for a smooth rotation. A metal spring is used to connect the chopper wheel's metal rod to the ceramic rod. All components are attached to a stainless steel platform for sturdiness and for ease of insertion into a tube furnace. During thermal tests, all components of the experimental setup, except the chopper wheel, are inserted in a tube furnace. Figure 4 shows a close-up of the assembled sensor head and the target disc.



**Figure 4. Close-up of the assembled sensor head and the target disc.**

holding the various optical components in place. Set screws were used along the sensor head to hold the metal spacers in place. The front (outer) surface of the sapphire window serves as the reference mirror (local oscillator) for the common-path interferometer.



**Figure 5. Interior of the sensor head.**

sensor head. A one-lens system was found to be the optimal setup for beam forming and collecting the reflected beams from measurement surfaces.

Figure 6 shows a photograph of the disk target used in this feasibility study. The disk has eight holes and eight recessed areas distributed evenly along the circumference of the target disc. These eight recessed areas were machined using a high precision computer-controlled mill and have depths ranging from 100 to 1500  $\mu\text{m}$  in 200  $\mu\text{m}$  increments. The disk is rotated using a ThorLabs MC1000A variable speed optical chopper (6,000 rpm maximum rotation speed) mounted on a precision translation stage to allow precise axial distance adjustment. OFDR measurements of the recessed areas of this disk were used to determine the basic characteristics of the method such as spatial resolution, measurement accuracy, measurement range, and sensitivity.

The light source used is a Ti:sapphire mode-locked laser with wavelength centered around 800 nm, having a spectral bandwidth of 27 nm FWHM, and

Figure 5 shows a schematic drawing of the interior of the 0.5 inch diameter sensor head. The outer shell of the sensor head is a 3 inch long stainless steel tube containing a clamshell-type fiber holder, sapphire lens (0.452 inch focal length), sapphire window (0.25 inch diameter, 0.125 inch thick), and metal spacers for separating and

Single-mode metal-coated fiber optic cable was used in the optical setup with only one end having a FC/APC fiber-optic connector. A solution of nitric acid with water was used to remove a portion of the copper coating to expose the bare fiber on the other distal end of the cable. After removing a portion of the copper coating, the bare fiber was cleaved using a typical cleaving tool. This cleaved end is positioned to send an optimum beam spot into the measurement surface and to collect the reflected laser beam. A clamshell-type fiber holder is used to center the fiber optic cable within the



**Figure 6. Photograph of target disc.**

total available power of 300 mW. The laser light is coupled to a common path fiber interferometer constructed using a 50/50 fiber coupler connected to a sensor head. Laser power out of the splitter is around 10-15 mW. A metal-coated fiber is attached to one end of the splitter, and the power output of this fiber is typically 5 mW. This laser is used for convenience and can easily be replaced by a broadband superluminescent diode. Spectral interferograms at the output of the common path interferometer are detected using a line scan camera (Atmel, 1,024 pixels, 12-bit digitization, frame rate of 50 kHz) coupled to a spectrograph (Spectra Physics, 1/4 m, 1,200 gr/mm). The spectral interferograms from the camera are acquired using a CameraLink frame grabber and transferred to a personal computer for further processing. In-house software processes the raw spectral interferograms by converting them to the appropriate form (amplitude versus frequency waveform), and performing the Fourier Transform to obtain the reflectogram. The detection system speed is limited by the current camera line scan rate and allows one measurement in about 20  $\mu$ s.

#### IV. Results and Discussion

##### A. Sensitivity, Spatial Resolution, Measurement Accuracy and Range

A sample 2-D image in frequency space is shown in Fig. 7. In the vertical time axis is composed of 4,096 individual spectral interferograms, covering 86 ms of data with an exposure time of 20  $\mu$ s per interferogram. Horizontal slices of the 2-D image are individual spectral interferograms, i.e. the intensity on each of the 1,024 pixels on the line scan camera. An interferogram from the 2-D image is shown in Fig. 8. Upon applying a Fast-Fourier Transform (FFT) to the interferogram, a depth profile is obtained and shown in Fig. 9. In this figure, the horizontal axis shows the depth in micrometers, and the vertical axis shows the intensity in arbitrary units. The spatial resolution is easily obtained from this figure by determining the FWHM of the peak.

Neutral density filters, with nominal ND of 0.5, 1.0, 2.0, 3.0 and 4.0, were used to determine the sensitivity of the system. These filters were calibrated by measuring the laser power with and without the filter in front of a power meter. The optical density and attenuation level (dB) of these filters were then determined. The laser power was first adjusted to the near-saturation limit of the detector. The filter is placed between a mirror surface (sample) and a window of the sensor. The interference fringes were optimized for each of the filters. Plotting the signal and noise level (in dB) versus attenuation in the sample arm (dB) provides the sensitivity of the instrument of about 60 dB. After applying correction for distance, the sensitivity of the instrument is 80dB. Wavelength calibration of the line scan camera sensor was performed using an Argon lamp to obtain a relationship between the wavelengths and pixel number of the camera. This calibration is necessary to obtain the absolute distance via the Fourier Transform.

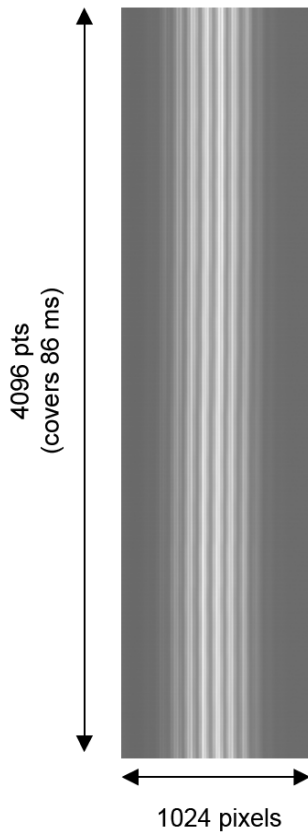


**Figure 7. Spectral image (stack of interferograms).**

The current setup of the instrument provided a spatial resolution of about 10  $\mu$ m. This was determined at the FWHM of the peak from several depth profiles such as shown in Fig. 9. The measured spatial resolution is well within the theoretical value, as obtained by the spectral bandwidth of the light source.

The rotating disk with eight recessed areas (ranging from 100 to 1500  $\mu$ m deep, with 200  $\mu$ m increment) was used to determine the clearance measurement range. The disk was spun at 100 Hz. At least four of the recessed areas could be seen in the collected 2-D image, as shown in Fig. 10. These images are the result of applying FFT to the spectral interferograms. Not all the recessed areas were seen because we have reached the theoretical limit of the measurement range given the current setup. Using Eq. 3 and the current system parameters, the theoretical measurement range is 1885  $\mu$ m. The measurement range is about 900  $\mu$ m. Note that this is half of the theoretical limit since we are using a common path interferometer and a mirror image is always obtained. This is characteristic of Fourier Domain ranging and imaging methods, where the Fourier Transform does not preserve phase information. This leads to mirror images across the reference plane. This means only half of the theoretical range can be used. The range can be extended by employing a camera with more pixel resolution.

We obtained multiple measurements of the recessed areas and determined the sensor precision to be  $\pm 6$   $\mu$ m. The accuracy of the sensor depth measurement

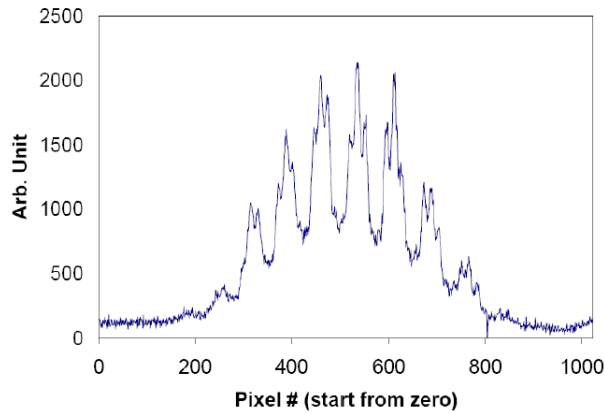


**Figure 8. Individual interferogram.**

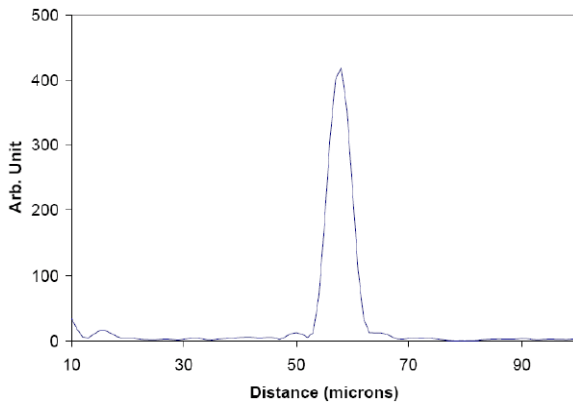


**Figure 9. Depth profile.**

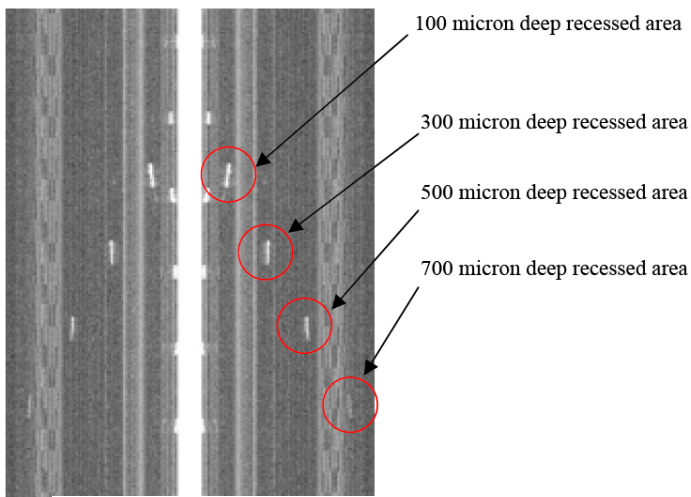


**Figure 10. Spatial image (stack of depth profiles).**

was determined by comparison to measurements with a depth micrometer that has an accuracy of  $\pm 2 \mu\text{m}$ . The accuracy of the sensor is  $\pm 4 \mu\text{m}$ .

### B. Thermal Effects

The maximum operating temperature for the copper-coated fibers was verified using a low-temperature tube furnace (capable of operating at  $1100^\circ\text{C}$ ). A fiber laser source (Thorlabs, Model S1FC763, at 2 mW) operating at 763 nm was used to monitor the light transmission through the copper-coated fiber during the heating process. Light output at one end of the fiber was monitored for signs of internal breakage (i.e., loss of light transmission). The ends of the furnace were covered with thermal blankets to minimize heat loss.

In the first thermal test, the copper-coated fiber optic cable was heated from  $600$  to  $900^\circ\text{C}$  in  $50^\circ\text{C}$  increment. The fiber failed at  $900^\circ\text{C}$ . Temperature was held for 10 minutes at each operating point. After cooling down to room temperature, the fiber was extremely brittle to the touch. The fiber broke into several sections when gently tapped.

In the second thermal test, a one inch portion of the copper-coating was removed using a solution of nitric acid and water. This exposed section of the fiber was centered inside the furnace. The copper-coated fiber was heated from  $200$  to  $600^\circ\text{C}$  in  $100^\circ\text{C}$  increment, and from  $600$  to  $800^\circ\text{C}$  in  $50^\circ\text{C}$  increment. Temperature was held for 10 minutes at each operating point, except at  $800^\circ\text{C}$  where it was held for 60 minutes. There was no loss of light at all temperatures. However, the fiber was extremely brittle to the touch, just like the first test.

In the third thermal test, the copper-coated fiber was heated at  $600^\circ\text{C}$  for 60 minutes. Upon cooling down to room temperature, the fiber remained flexible. To operate these metal-coated fibers beyond  $600^\circ\text{C}$ , active cooling with air or water will be necessary to maintain the physical integrity.

Having determined the operating temperature of the metal-coated fibers OFDR measurements were performed at elevated temperatures. The prototype sensor was suspended inside a high-temperature furnace using two ceramic rods on optical mounts, as shown in Fig. 11. All sensor components except the chopper were inserted into the oven. The temperature inside the oven was monitored using a thermocouple. The ends of the oven were covered with

thermal blankets to minimize heat loss from these openings. Measurements of the recessed regions were first conducted without any heat load. The temperature was then brought to a specified level and data were collected.

When the device had equilibrated with the oven temperature, the temperature was increased by another 100°C. The temperature ranges from room temperature to 600°C. At temperatures above 200°C, the sensor became misaligned, possibly due to thermal expansion of the components inside the sensor head. Upon cooling down to room temperature, the recessed areas could be seen again on the computer screen. Better management of thermal expansion within the sensor head is necessary for future development of the sensor.

In the final thermal test, a one-foot section of the copper-coated fiber was heated from room temperature to 600°C. The sensor head and target disk were outside the oven and at room temperature. A mirror was placed in front of the sensor head at some distance to generate a spectral interferogram. Spectral interferograms were collected at every 100°C increment. As shown in Fig. 12, the results at room temperature, 300°C, and 600°C indicate that the quality of the spectral interferograms and the intensity of the signals were not degraded by heating a section of the fiber.

### C. Sooting Effects

The effects of optics contamination were investigated by applying graphite powder (to simulate soot from flames) on the optical window of the sensor, and the mirror used as the reflecting surface, see Fig. 13. We collected two spectral interferograms with and without soot on the optical surfaces. Figure 14 shows that there is no substantial loss of signal intensity, but there is degradation in the quality of the optical fringes as a result of applying soot on the optical surfaces. Further studies of the effect of soot on the accuracy and precision are planned.

### D. Envisioned Tip Clearance Sensor

Figure 15 shows a schematic of an envisioned tip clearance sensor for implementation into an engine test stand. An optical switch will be used to allow the probing of multiple locations using the same light source and detector. The prototype instrument will have two sensor heads, having an outer diameter of less than 0.5 inch. The probe will be designed to withstand temperatures up to 600°C without active cooling. The copper-coated fibers are shown to operate well at this temperature. Operation at higher temperature will require active cooling using air or water for now. Fiber optic technologies are progressing fast, single-mode fibers that can operate at high temperatures will be available in the future. We determined a 600°C operation limit without external cooling for metal clad optical fibers currently available. Sapphire optical fibers can operate beyond 1,000°C, but their multi-mode property is not well-suited for this sensor. Off-the-shelf electronic components such as broadband light sources (super luminescence diode), line scan camera with high-resolution and short exposure time, spectrometer, fiber optic cables, frame grabbers will be used. The measurement system will be self-contained, having a software interface with measurement analyses and display. The measurement range will be 2,000 μm with a 10 μm or better spatial resolution. Longer depth ranges are possible, but at the



**Figure 11. Tube furnace with experimental setup inside.**

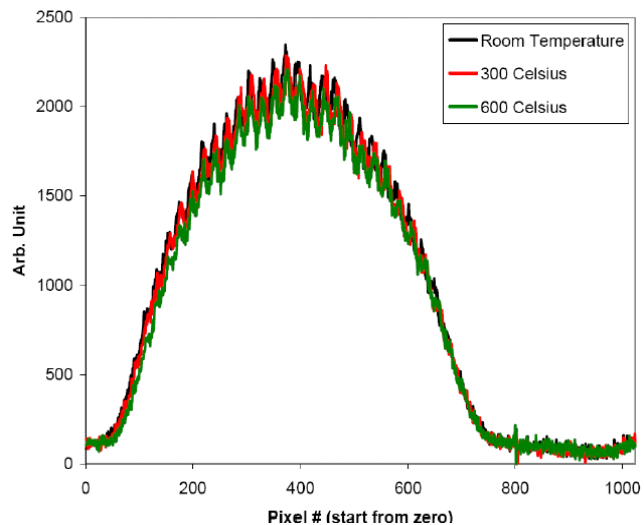


**Figure 12. Temperature effects on spectral interferogram.**



**Figure 13. Soot deposits on optical surfaces.**

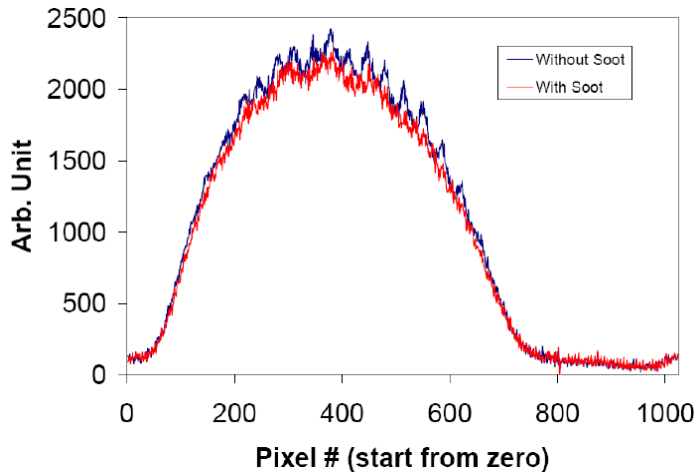


**Figure 14. Soot deposits on spectral interferogram.**

To synchronize with the rotational speed of the blades within a stage, the same light source used for tip clearance measurement can be used with a silicon photodiode detector to record the time of arrival of each blade at the measurement location. In addition blade tip timing data can be used for the measurement of blade vibrations.

expense of the spatial resolution.

Based on currently available line scan cameras, a measurement rate of at least 100 kHz and up to 200 kHz is achievable. A typical blade tip speed is 400 m/s and for a blade width of 1 mm the blade tip exposure time at the measurement location is 2.5  $\mu$ s. This corresponds to a 400 kHz camera frame rate in order to capture each passing blade. The maximum line scan rate of cameras is progressing rapidly as well. For example, a Basler line scan camera with a maximum rate of 217 kHz using 512 pixels, giving an exposure time of 3.4  $\mu$ s is available. For wider turbine blade tips (widths of ~2 mm and above) the Basler camera would permit the measurement of individual passing blade tip without occasionally missing a blade tip passage.

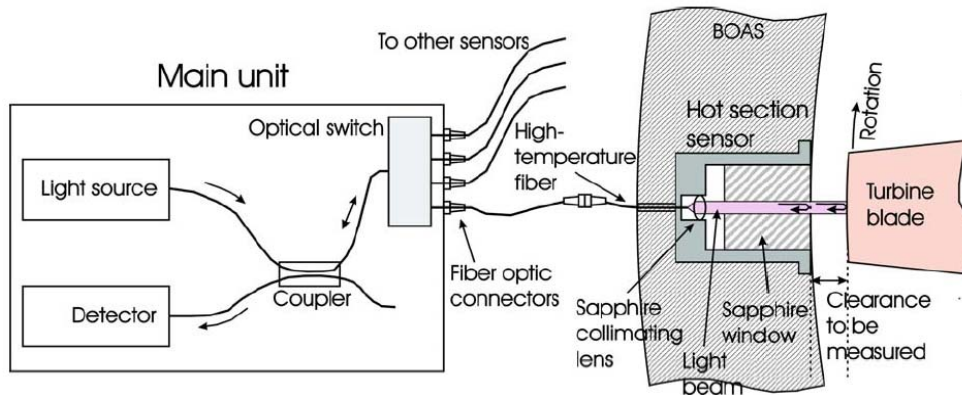


**Figure 15. Envisioned blade tip clearance sensor system.**

## V. Summary

A prototype sensor for measuring tip clearances was built and tested. Measurements were conducted in both room temperature and inside a tube furnace. The spatial resolution of the sensor was 10  $\mu$ m, and measurement accuracy of 4  $\mu$ m was obtained. A measurement range of less than 1 mm was obtained. This is sufficient for most practical applications in turbine engines since the tip clearances range from 250-750  $\mu$ m. A future prototype tip clearance sensor, having multiple sensor heads, was described.

This sensor system will provide a new tool for engine manufacturers to study and optimize blade tip clearance with high accuracy without the need for repetitive and cumbersome calibration procedures. Moreover, engine health monitoring and control systems will benefit from this sensor system for real-time implementation of active tip clearance control mechanisms in gas turbine engines. The envisioned compact, low weight and cost, high-temperature, self-calibrating sensor heads can be easily integrated into engine casings at several physical locations with minimal or no disturbance to the engine internal flow paths; thus, a flight-version of this sensor system is certainly within reach as well. This optical ranging technology will be useful for maintenance of commercial and

military aircraft, and industrial turbines. The instrument can be very useful for other applications that require rapid measurement of the distance between two surfaces at close proximity (millimeter range) with high accuracy (micrometer range).

### **Acknowledgments**

This material is based upon work supported by NASA under Contract No. NNX08CA63P. The NASA technical monitor for this project is Mark Woike.

### **References**

- <sup>1</sup>S. B. Lattime, and B. M. Steinetz, "Turbine Engine Clearance Control Systems: Current Practices and Future Directions," NASA TM 2002-211794, AIAA 2002-3790 (2002).
- <sup>2</sup>S. B. Lattime, B. M. Steinetz, and M. G. Robbie, "Test Rig for Evaluation Active Turbine Blade Tip Clearance Control Concepts," NASA TM-2003-212533, AIAA 2003-4700 (2003).
- <sup>3</sup>E. B. Holmquist, and P. L. Jalbert, "Turbine blade tip clearance measurement instrumentation," ASME Paper GT2007-27393 (2007).
- <sup>4</sup>L. Buttner, T. Pfister, and J. Czarske, "Fiber-optic laser Doppler turbine tip clearance probe," Opt. Lett. 31, 1217-1219 (2006).
- <sup>5</sup>K. Takada, T. Kitagawa, M. Shimizu, and M. Horiguchi, "High-sensitivity low coherence reflectometer using erbium-doped superfluorescent fiber source and erbium-doped power amplifier," Electron. Lett. 29, 365-367 (1993).
- <sup>6</sup>U. Glombitza, and E. Brinkmeyer, "Coherent Frequency-Domain Reflectometry for Characterization of Single-Mode Integrated-Optical Waveguides," J. Lightwave Technol. 11, 1377-1384 (1993).
- <sup>7</sup>R. Passy, N. Gisin, J. P. Von der Weid, and H. H. Gilgen, "Experimental and Theoretical Investigations of Coherent OFDR with Semiconductor Laser Sources," J. Lightwave Technol. 12, 1622-1630 (1994).
- <sup>8</sup>J. P. Von der Weid, R. Passy, and N. Gisin, "Mid-Range Coherent Optical Frequency Domain Reflectometry with a DFB Laser Diode Coupled to an External Cavity," J. Lightwave Technol. 13, 954-960 (1995).
- <sup>9</sup>P. Oberson, B. Huttner, O. Guinnard, L. Guinnard, G. Ribordy, and N. Gisin, "Optical Frequency Domain Reflectometry with a Narrow Linewidth Fiber laser," IEEE Photon. Technol. Lett. 12, 867-869 (2000).
- <sup>10</sup>A. B. Vakhnin, D. J. Kane, W. R. Wood, and K. A. Peterson, "Common path interferometer for frequency-domain optical coherence tomography," Appl. Opt. 42, 6953-6958 (2003).